






Quantum geometric tensor and quantum phase transitions in the Lipkin-Meshkov-Glick modelDaniel Gutiérrez-Ruiz ^{1,*}, Diego Gonzalez ^{1,2,†}, Jorge Chávez-Carlos ^{3,‡}, Jorge G. Hirsch ^{1,§} and J. David Vergara ^{1,||}¹*Instituto de Ciencias Nucleares, Universidad Nacional Autónoma de México, Apartado Postal 70-543, Ciudad de México 04510, México*²*Departamento de Física, Cinvestav, Avenida Instituto Politécnico Nacional 2508, San Pedro Zacatenco, 07360 Gustavo A. Madero,**Ciudad de México, México*³*Instituto de Ciencias Físicas, Universidad Nacional Autónoma de México, Cuernavaca, Morelos 62210, México*

(Received 26 January 2021; revised 15 April 2021; accepted 27 April 2021; published 10 May 2021)

We study the quantum metric tensor and its scalar curvature for a particular version of the Lipkin-Meshkov-Glick model. We build the classical Hamiltonian using Bloch coherent states and find its stationary points. They exhibit the presence of a ground-state quantum phase transition where a bifurcation occurs, showing a change in stability associated with an excited-state quantum phase transition. Symmetrically, for a sign change in one Hamiltonian parameter, the same phenomenon is observed in the highest-energy state. Employing the Holstein-Primakoff approximation, we derive analytic expressions for the quantum metric tensor and compute the scalar and Berry curvatures. We contrast the analytic results with their finite-size counterparts obtained through exact numerical diagonalization and find excellent agreement between them for large sizes of the system in a wide region of the parameter space except in points near the phase transition where the Holstein-Primakoff approximation ceases to be valid.

DOI: [10.1103/PhysRevB.103.174104](https://doi.org/10.1103/PhysRevB.103.174104)**I. INTRODUCTION**

The geometry of quantum phase transitions is a vast and exciting subject (see Ref. [1] for a comprehensive and recent review). A fundamental structure that characterizes a quantum system's geometry is the *quantum geometric tensor* (QGT). This quantity, introduced by Provost and Valle [2], is useful to measure the distance in the parameter space between two quantum states with infinitesimally shifted parameters. Experimental protocols to measure its components have been proposed in Refs. [3,4] and were carried out in Ref. [5] by exploiting the relation between the QGT and the response of quantum systems under periodic modulations. In the context of topological phase transitions and topological invariants, the quantum geometric tensor plays an important role and has been measured [6,7]. The critical scaling behavior of its components has been analyzed in Refs. [8,9].

From its definition, it has been recognized that the QGT has a divergent behavior at points in parameter space that induce level crossings and, therefore, that is useful to detect quantum phase transitions (QPTs) [10]. QPTs occur at zero temperature and are characterized by a change in the ground state's analytic properties induced by quantum fluctuations. From a theoretical standpoint, the QGT can be obtained through a second-order expansion of the distance induced by the *fidelity*, a well-known tool in information theory. This quantity has an abrupt change in a quantum phase transition, and it has been

used extensively (see Refs. [11–13] and references therein). Moreover, alternative definitions of the fidelity and machine learning approaches have recently been used to study phase transitions on spin models with Hamiltonians depending on parameters [14]. Mathematically, the fidelity emerges from the Fubini-Study distance, which is defined in the projective Hilbert space and is a measure of statistical indistinguishability between pure or mixed quantum states [15].

In the general formulation of Ref. [2], the QGT includes in its real part the quantum metric tensor (QMT) and in its imaginary part the Berry curvature. The study of the geometric structures that emerge from the QMT has been carried out in various systems. Geodesics were studied in Refs. [9,16,17], and an analysis of singularities and their relation with topology for the ground state was performed in Refs. [18,19].

A specific geometric structure that stands out is the *scalar curvature* (or *Ricci scalar*), a local invariant that quantifies the deviation of the space of parameters from being Euclidean. Consequently, the value of the scalar curvature at a point is independent of the parameter space coordinates that were employed to calculate the metric and, hence, can be used to identify whether or not a singularity in the metric is genuine or coordinate dependent. In quantum mechanics, one can naturally compute the scalar curvature of the QMT and observe its behavior as a function of the parameters, particularly, at a region in parameter space where a QPT occurs. In the thermodynamic limit of a transverse *XY* spin chain it was found that the scalar curvature is an indicator of the QPT [10], whereas in the Dicke model of quantum optics the scalar curvature does not show any particular behavior, but the QMT diverges at the QPT [20]. This contrasts strongly with classical (thermodynamic) phase transitions where a Riemannian metric can also be defined [21,22], and its corresponding scalar curvature shows a singularity in the thermodynamic space across the

*daniel.gutierrez@correo.nucleares.unam.mx

†dgonzalez@fis.cinvestav.mx

‡jchavez@icf.unam.mx

§hirsch@nucleares.unam.mx

||vergara@nucleares.unam.mx

phase transition [23,24]. It is also at variance with the behavior of the fidelity susceptibility, which is a component of the QMT and exhibits a peak at the QPT in the Dicke model for a finite number of particles [25,26] and in the vicinity the Berezinskii-Kosterlitz-Thouless QPT in one-dimensional systems for finite sizes [27] and in the thermodynamic limit [27–29].

In what follows, we consider the Lipkin-Meshkov-Glick (LMG) model [30–32] and analyze in detail the behavior of the QMT and its scalar curvature, in the thermodynamic limit and for finite sizes of the system. Some of the fidelity susceptibility components at the quantum stationary points have been studied varying one of the Hamiltonian parameters [13,33–35]. In Refs. [20,36] it was found that for the standard version of the LMG model the fidelity metric is ill defined at zero temperature. We extend these studies in the present paper by including in the LMG Hamiltonian two terms linear in the angular momentum components. This extended model has a well-defined QMT, whose characteristics and relationship with the QPT are studied in detail employing both analytical and numerical methods. In particular, we perform a meticulous analysis of the scalar curvature, and we show some of the exciting properties that this geometric invariant has in the QPT.

The paper is organized as follows. In Sec. II, we introduce the mathematical tools employed in the study of the geometry of the Hamiltonian parameter space. In Sec. III, we present the LMG model, the Hamiltonian, its semiclassical limit, stationary points, and quantum phases employing $SU(2)$ coherent states. The geometry of the parameter space of the LMG model is studied in Sec. IV for the ground state and the highest-energy state, including the quantum metric tensor and the scalar curvature. Analytic expressions derived employing the truncated Holstein-Primakoff expansion are compared with numerical calculations for various system dimensions. Conclusions are discussed in Sec. V. The Appendix shows the difficulties found in evaluating the scalar curvature employing coherent states.

II. GEOMETRY OF THE PARAMETER SPACE

Consider a quantum system whose Hamiltonian $\hat{H}(x)$ depends smoothly on a set of m real adiabatic parameters denoted by $x = \{x^i\}$ ($i = 1, \dots, m$), which parametrize some m -dimensional parameter manifold \mathcal{M} . For an orthonormal eigenvector $|n(x)\rangle$ of the system with nondegenerate eigenvalue $E_n(x)$, the QGT is defined by [2]

$$Q_{ij}^{(n)} := \langle \partial_i n | \partial_j n \rangle - \langle \partial_i n | n \rangle \langle n | \partial_j n \rangle, \quad (1)$$

where $\partial_i := \frac{\partial}{\partial x^i}$. The QGT transforms as a covariant tensor of rank two and is invariant under the $U(1)$ gauge transformation $|n(x)\rangle \rightarrow e^{i\alpha_n(x)} |n(x)\rangle$ with $\alpha_n(x)$ as a smooth function of the parameters. The (symmetric) real part of the QGT yields the QMT [2],

$$g_{ij}^{(n)} = \text{Re } Q_{ij}^{(n)}, \quad (2)$$

which is a Riemannian metric and provides the distance $\delta\ell^2 = g_{ij}^{(n)}(x) \delta x^i \delta x^j$ between the quantum states $|n(x)\rangle$ and $|n(x + \delta x)\rangle$, corresponding to infinitesimally different parameters. The (antisymmetric) imaginary part of the QGT encodes

the Berry curvature [37],

$$F_{ij}^{(n)} = -2 \text{Im } Q_{ij}^{(n)}, \quad (3)$$

which, after being integrated over a surface subtended by a closed path in the parameter space, gives rise to the geometric Berry phase [37].

An important aspect of the QGT is that its singularities are associated with QPTs [8,10]. To gain a better understanding of this aspect, let us write the QGT in a perturbative form. Inserting the identity operator $\mathbb{I} = \sum_m |m\rangle \langle m|$ in the first term of Eq. (1) and using

$$\langle m | \partial_i n \rangle = \frac{\langle m | \partial_i \hat{H} | n \rangle}{E_n - E_m} \quad \text{for } m \neq n, \quad (4)$$

which follows from the eigenvalue equation $\hat{H} |n\rangle = E_n |n\rangle$, the QGT takes the form [13]

$$Q_{ij}^{(n)} = \sum_{m \neq n} \frac{\langle n | \partial_i \hat{H} | m \rangle \langle m | \partial_j \hat{H} | n \rangle}{(E_m - E_n)^2}. \quad (5)$$

This expression shows that at the stationary points of the QPT, which are characterized by the ground-state level crossing, the components of the QGT (and, hence, the components of the QMT and the Berry curvature) are singular. In general, it is clear from Eq. (5) that the components of the QGT are singular at the points where the parameters take a value of $x^* \in \mathcal{M}$ such that $E_n(x^*) = E_m(x^*)$.

To determine whether or not the QMT has a genuine singularity, i.e., a singularity that cannot be removed by changing coordinates, we can use the scalar curvature, which is independent of the coordinates that were chosen to parametrize the manifold \mathcal{M} . For a two-dimensional manifold \mathcal{M} endowed with the Riemannian QMT, which is the case of interest in this paper, the scalar curvature R can be computed using the expression,

$$R = \frac{1}{\sqrt{|g|}} (\mathcal{A} + \mathcal{B}), \quad (6)$$

where $g = \det[g_{ij}]$ and we have defined the quantities \mathcal{A} and \mathcal{B} by

$$\begin{aligned} \mathcal{A} &:= \partial_1 \left(\frac{g_{12}}{g_{11} \sqrt{|g|}} \partial_2 g_{11} - \frac{1}{\sqrt{|g|}} \partial_1 g_{22} \right), \\ \mathcal{B} &:= \partial_2 \left(\frac{2}{\sqrt{|g|}} \partial_1 g_{12} - \frac{1}{\sqrt{|g|}} \partial_2 g_{11} - \frac{g_{12}}{g_{11} \sqrt{|g|}} \partial_1 g_{11} \right). \end{aligned} \quad (7)$$

In what follows, we analyze the Riemannian curvature of the LMG model, which in this case is contained in the scalar curvature, and how it changes across a quantum phase transition and the information it offers.

III. LMG MODEL

The LMG model [30–32] was originally employed as a tool to describe the shape phase transition in nuclei and at the same time to explore the limits of different approximate methods [38–41], taking advantage of its simplicity. It provides a description of the collective modes of systems with two degrees of freedom, such as a single particle evolving in a double-well potential or an interacting two-level boson system and includes one- and two-body interactions, which can be mapped

to a quantum top in a constant magnetic field [42,43]. It has been useful in the description of a wide variety of many-body systems: spin systems with infinite-range interactions [44], quantum superpositions of Bose-Einstein condensates [45], and single molecular magnets [46,47]. In recent years this fully connected model provided the testing ground to explore novel properties, such as time-translation symmetry breaking and time crystals [48], and the dynamics around the ground state and the excited quantum phase transitions, including quantum driving and control [49], dynamical scaling behavior across adiabatic quantum phase transitions [50,51], quench dynamics [52], and nonadiabatic dynamics [53], which were experimentally studied employing trapped atoms [54].

The scaling properties of the entanglement at quantum phase transition in the LMG model were studied in detail by Vidal and co-workers [55–58]. The LMG model is part of an extended family of exactly solvable Hamiltonians, which can be built using a complete set of mutually commuting quantum invariants of a generalized Gaudin Lie algebra [59]. Employing spin coherent states, detailed analysis of the quantum phases [60,61], and the order of the respective phase transitions have been performed [62]. Having a finite Hilbert space, the complete energy spectrum of the LMG model can be obtained through a numerical diagonalization for a large number of individual spins [63]. Although the ground state has two quantum phases, there is a divergence of the density of states at the threshold energy [64,65], and the complete spectrum has four qualitatively different regions in the parameter space [66]. This divergence is a paradigmatic example of an excited-state quantum phase transition (ESQPT) [67–73]. At this energy, the LMG has a positive Lyapunov exponent, which is not a signature of chaos but an instability where the quantum out-of-time-order correlator also exhibits an exponential growth [74].

The quantum criticality of the LMG model has been studied, varying one of the Hamiltonian parameters employing the fidelity susceptibility [13,33–35]. The relationship between the information geometry and the quantum phase transitions was explored in the Dicke model, showing that the scalar curvature is continuous across the phase-transition boundary [20]. In the same work, it was found that, for the standard version of the LMG model, the metric’s determinant is zero, signaling that information geometry is ill defined in this model. In Ref. [36] the authors concluded that due to the integrability of the isotropic LMG model, ground-state level crossings occur, leading to an ill-defined fidelity metric at zero temperature. To avoid these difficulties, we included in Hamiltonian (8) two terms linear in the angular momentum components. As is shown below, this provides a richer model with interesting properties worth being explored.

The LMG model [30–32] describes the collective motion of a set of N two-level systems mutually interacting. In this paper, we will consider the following Hamiltonian:

$$\hat{H}_{\text{LMG}} = \Omega \hat{J}_z + \Omega_x \hat{J}_x + \frac{\xi_y}{j} \hat{J}_y^2, \quad (8)$$

where $\hat{J}_{x,y,z} = (1/2) \sum_{n=1}^N \sigma_{x,y,z}^{(n)}$ are the collective pseudospin operators given by the sum of the Pauli matrices $\sigma_{x,y,z}^{(n)}$ for each two-level system n and $j = N/2$ with j coming from the

eigenvalue $j(j+1)$ of the total spin operator $\hat{J}^2 = \hat{J}_x^2 + \hat{J}_y^2 + \hat{J}_z^2$ and, thus, gives the size of the system. Also, Ω is the energy difference of the two-level systems, Ω_x and ξ_y are parameters, and we put $\hbar = 1$.

A. Semiclassical analysis

The classical LMG Hamiltonian is obtained by taking the expectation value of \hat{H}_{LMG}/j on Bloch coherent states $|z\rangle = (1 + |z|^2)^{-j} e^{z\hat{J}_+} |j, -j\rangle$, where $|j, -j\rangle$ is the state with the lowest pseudospin projection and \hat{J}_+ is the raising operator.

Defining $z = \tan(\frac{\theta}{2})e^{-i\phi}$, the classical LMG Hamiltonian has the simple form

$$h_{\text{LMG}} = \frac{\langle z | \hat{H}_{\text{LMG}} | z \rangle}{j} = -\Omega \cos \theta + \Omega_x \sin \theta \cos \phi + \xi_y \sin^2 \theta \sin^2 \phi. \quad (9)$$

It can also be written in terms of the canonical variables,

$$Q = \sqrt{2(1 - \cos \theta)} \cos \phi, \\ P = -\sqrt{2(1 - \cos \theta)} \sin \phi, \quad (10)$$

and reads

$$h_{\text{LMG}}(Q, P) = \frac{\Omega}{2}(Q^2 + P^2) - \Omega + \Omega_x Q \sqrt{1 - \frac{Q^2 + P^2}{4}} + \xi_y P^2 \left(1 - \frac{Q^2 + P^2}{4}\right). \quad (11)$$

Note that Hamiltonian (9) is invariant under the interchange $\phi \leftrightarrow -\phi$, which reflects in Hamiltonian (11) in the symmetry under the interchange $P \leftrightarrow -P$. It implies that all stationary points are doubly degenerate if $\phi \neq 0$ or π ($P \neq 0$).

The allowed domain for the parameters is $\Omega, \Omega_x, \xi_y \in \mathbb{R}$. To simplify the analysis, we consider only two independent parameters of the system, setting from now on $\Omega = 1$ (i.e., we measure the energies in units of Ω).

1. Stationary points

For the classical Hamiltonian (11) we obtain the equations of motion,

$$\dot{Q} = \frac{\partial h_{\text{LMG}}}{\partial P} = \frac{P}{2} \left[2 - \xi_y (2P^2 + Q^2 - 4) - \frac{\Omega_x Q}{\sqrt{4 - (P^2 + Q^2)}} \right], \\ \dot{P} = -\frac{\partial h_{\text{LMG}}}{\partial Q} = \frac{1}{2} \left[\xi_y P^2 Q + \frac{\Omega_x Q^2}{\sqrt{4 - (P^2 + Q^2)}} - \Omega_x \sqrt{4 - (P^2 + Q^2)} - 2Q \right]. \quad (12)$$

The stationary points correspond to vanishing phase space velocities (\dot{Q}, \dot{P}) in the region $0 \leq \theta \leq \pi$, $0 \leq \phi \leq 2\pi$. The

valid solutions are

$$\begin{aligned} \mathbf{x}_1 &= (Q_1, P_1) \\ &= \left(\sqrt{2 + \frac{2}{\sqrt{\Omega_x^2 + 1}}}, 0 \right) \text{ with} \\ (\theta_1, \phi_1) &= \left(\arccos \left(\frac{1}{\sqrt{\Omega_x^2 + 1}} \right), 0 \right), \end{aligned} \quad (13)$$

$$\begin{aligned} \mathbf{x}_2 &= (Q_2, P_2) \\ &= \left(-\sqrt{2 - \frac{2}{\sqrt{\Omega_x^2 + 1}}}, 0 \right) \text{ with} \\ (\theta_2, \phi_2) &= \left(\arccos \left(\frac{1}{\sqrt{\Omega_x^2 + 1}} \right), \pi \right), \end{aligned} \quad (14)$$

if $\xi_y \leq -\frac{\sqrt{1+\Omega_{xc}^2}}{2}$,

$$\mathbf{x}_3 = (Q_3, P_3) = \left(-\frac{\Omega_x}{\sqrt{\xi_y(2\xi_y - 1)}}, -\frac{\sqrt{-\Omega_x^2 + 4\xi_y^2 - 1}}{\sqrt{\xi_y(2\xi_y - 1)}} \right),$$

with

$$(\theta_3, \phi_3) = \left(\arccos \left(-\frac{1}{2\xi_y} \right), -\arccos \left(\frac{\Omega_x}{\sqrt{4\xi_y^2 - 1}} \right) \right), \quad (15)$$

and

$$\mathbf{x}'_3 = (Q_3, P_3) = \left(-\frac{\Omega_x}{\sqrt{\xi_y(2\xi_y - 1)}}, \frac{\sqrt{-\Omega_x^2 + 4\xi_y^2 - 1}}{\sqrt{\xi_y(2\xi_y - 1)}} \right)$$

with

$$(\theta'_3, \phi'_3) = \left(\arccos \left(-\frac{1}{2\xi_y} \right), \arccos \left(\frac{\Omega_x}{\sqrt{4\xi_y^2 - 1}} \right) \right), \quad (16)$$

if $\xi_y \geq \frac{\sqrt{1+\Omega_{xc}^2}}{2}$,

$$\mathbf{x}_4 = (Q_4, P_4) = \left(\frac{\Omega_x}{\sqrt{\xi_y(2\xi_y - 1)}}, -\frac{\sqrt{-\Omega_x^2 + 4\xi_y^2 - 1}}{\sqrt{\xi_y(2\xi_y - 1)}} \right),$$

with

$$(\theta_4, \phi_4) = \left(\arccos \left(\frac{1}{2\xi_y} \right), -\arccos \left(\frac{\Omega_x}{\sqrt{4\xi_y^2 - 1}} \right) \right), \quad (17)$$

and

$$\mathbf{x}'_4 = (Q_4, P_4) = \left(\frac{\Omega_x}{\sqrt{\xi_y(2\xi_y - 1)}}, \frac{\sqrt{-\Omega_x^2 + 4\xi_y^2 - 1}}{\sqrt{\xi_y(2\xi_y - 1)}} \right),$$

with

$$(\theta'_4, \phi'_4) = \left(\arccos \left(\frac{1}{2\xi_y} \right), \arccos \left(\frac{\Omega_x}{\sqrt{4\xi_y^2 - 1}} \right) \right). \quad (18)$$

TABLE I. Classical energies at each stationary point.

Point	Energy
\mathbf{x}_1	$\sqrt{\Omega_x^2 + 1}$
\mathbf{x}_2	$-\sqrt{\Omega_x^2 + 1}$
\mathbf{x}_3	$(1 + \Omega_x^2)/(4\xi_y) + \xi_y$
\mathbf{x}_4	$(1 + \Omega_x^2)/(4\xi_y) + \xi_y$

2. Energy at the stationary points

The energies $e_i = h_{\text{LMG}}(\mathbf{x}_i)$ associated with each stationary point are listed in Table I.

These energy surfaces have interesting properties:

(1) They are symmetric under the interchange $\Omega_x \leftrightarrow -\Omega_x$.

(2) The energy e_3 is only defined in the region $\xi_y \leq -\frac{\sqrt{1+\Omega_{xc}^2}}{2}$ where it is negative and lower than e_2 .

(3) The energy e_4 is only defined in the region $\xi_y \geq \frac{\sqrt{1+\Omega_{xc}^2}}{2}$ where it is positive and higher than e_1 .

(4) The line $\xi_y = -\frac{\sqrt{1+\Omega_{xc}^2}}{2}$ is the *separatrix* between two quantum phases. The ground state is described by the coherent state \mathbf{x}_2 on one side of this line and by \mathbf{x}_4 on the other side. A similar situation occurs for the highest-energy state for $\xi_y = \frac{\sqrt{1+\Omega_{xc}^2}}{2}$: It is described by \mathbf{x}_4 in one phase and by \mathbf{x}_1 in the other phase. These energy surfaces are shown in Fig. 1.

(5) The energies are shown in Fig. 2 as functions of Ω_x for $\xi_y = -2.3$ in (a) and for $\xi_y = 2.3$ in (b). In both figures, the color code is red for e_1 , green for e_2 , orange for e_3 , and blue for e_4 .

In what follows, we limit the domain of ξ_y to positive values. Under this condition, the interesting stationary points are located at the top of the energy spectrum. Due to the symmetries in the model, reversing the sign of ξ_y would generate an analogous analysis for the ground state.

3. Observables

In Fig. 3, we show the expectation values of some observables in spin coherent states for the LMG model and compare them with the expectation values taken in the highest-energy

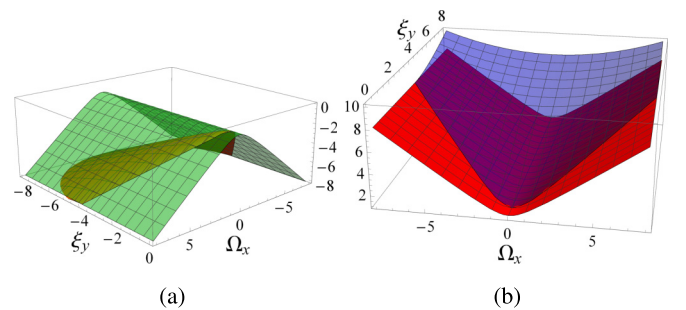


FIG. 1. (a) The two lower-energy surfaces e_2 (green) and e_3 (orange) as functions of the coupling parameters Ω_x and $\xi_y < 0$. (b) The two higher-energy surfaces e_1 (red) and e_4 (blue) as functions of the coupling parameters Ω_x and $\xi_y > 0$.

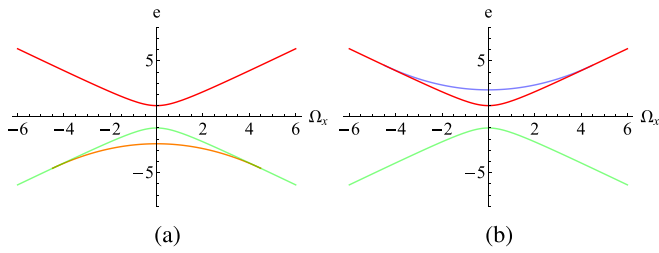


FIG. 2. Critical energies plotted as a function of the coupling parameter Ω_x for (a) $\xi_y = -2.3$ and (b) $\xi_y = 2.3$. The color code is e_1 (red), e_2 (green), e_3 (orange), and e_4 (blue).

eigenstate, obtained with a numerical diagonalization for $j = 128$ and $\xi_y = 2.3$. The quantum phase transition manifests as a discontinuity in the derivative of the plots at $\Omega_{xc} = 4.490$ for (b)–(d).

4. Instabilities and excited-state quantum phase transitions

The Hamiltonian (11) is integrable. The stationary points \mathbf{x}_3 and \mathbf{x}_4 are regular with the Lyapunov exponent equal to zero. When $\xi_y > \frac{\sqrt{1+\Omega_x^2}}{2}$, point \mathbf{x}_1 is unstable hyperbolic. The same happens for \mathbf{x}_2 when $\xi_y < -\frac{\sqrt{1+\Omega_x^2}}{2}$. In these cases, they have a positive Lyapunov exponent given by

$$\lambda = \sqrt{\sqrt{1 + \Omega_x^2} (2\xi_y - \sqrt{1 + \Omega_x^2})}. \quad (19)$$

Figure 4 shows the Lyapunov exponent as a function of the parameters Ω_x and $\xi_y > 0$.

Moving across the parameter space, it is possible to change the kind of stability of the stationary points of the Hamiltonian. In Fig. 5, we can see three points. For positive values of ξ_y , the green point corresponds to \mathbf{x}_2 , the ground state of the system, which remains a center point. On the other hand, the red point corresponds to \mathbf{x}_1 . It is hyperbolic as long as

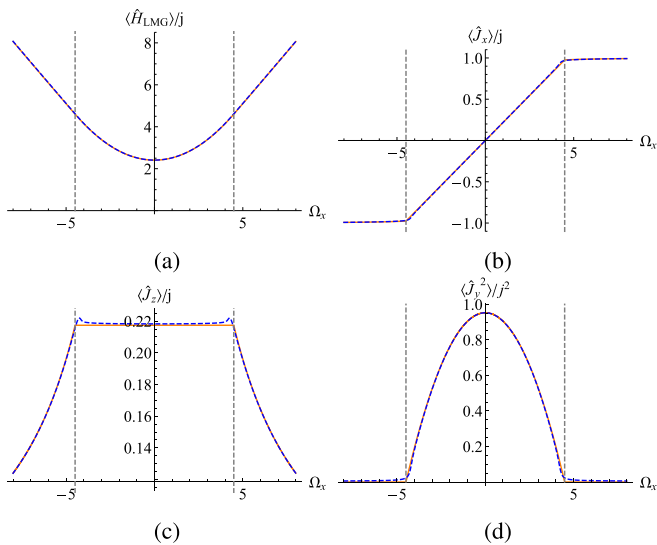


FIG. 3. Comparison of the expectation values of different observables taken in the highest-energy eigenstate (dashed blue) and in spin coherent states (solid orange) for $j = 128$ and $\xi_y = 2.3$.

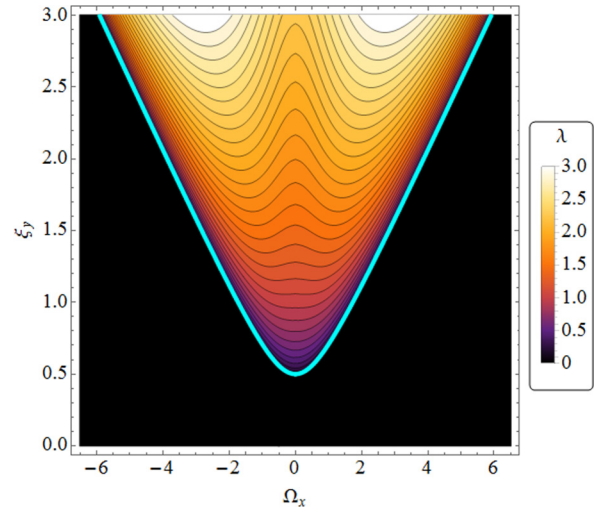


FIG. 4. Lyapunov exponent for the stationary point \mathbf{x}_1 as a function of the coupling parameters Ω_x and $\xi_y > 0$. The black zone indicates a null Lyapunov exponent.

$\Omega_x < \Omega_{xc}$, where Ω_{xc} satisfies $\xi_y = \frac{\sqrt{1+\Omega_{xc}^2}}{2}$ [Figs. 5(a) and 5(b)] and ends up merging with the two blue points \mathbf{x}_4 and \mathbf{x}'_4 when $\Omega_x > \Omega_{xc}$, becoming then a maximum (unstable) center point [Figs. 5(c) and 5(d)].

The phase transition appears when $\xi_y = \frac{\sqrt{1+\Omega_x^2}}{2}$. In the region $\xi_y > \frac{\sqrt{1+\Omega_x^2}}{2}$, \mathbf{x}_1 is a saddle point, associated with an

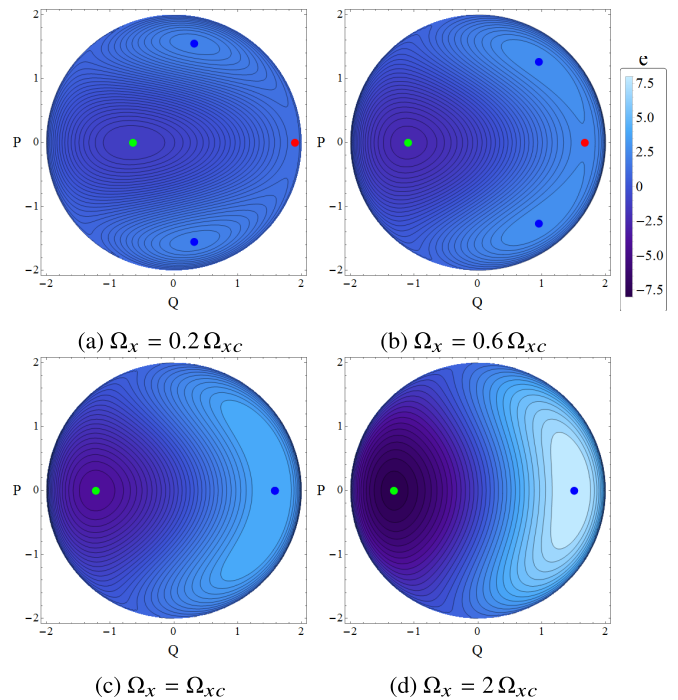


FIG. 5. Energy surfaces for different values of the parameters Ω with $\Omega_{xc} = \sqrt{4\xi_y^2 - 1}$ with $\xi_y = 2$. Green points are stable center points \mathbf{x}_2 , the blue ones are unstable center points: \mathbf{x}_4 and \mathbf{x}'_4 in (a) and (b), and in (c) and (d), the red point is the stationary point with positive Lyapunov exponent \mathbf{x}_1 , only present in (a) and (b).

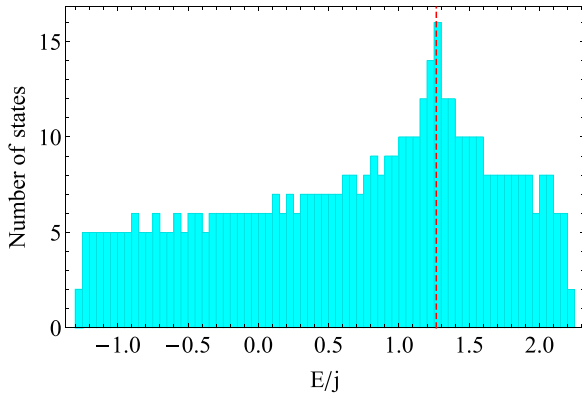


FIG. 6. Density of states when $\xi_y = 2$ and $\Omega_x = 0.2 \Omega_{xc}$ for $j = 256$. The red dashed line indicates the classical energy $e_1 = \sqrt{1 + \Omega_x^2} = 1.265$ where the ESQPT takes place.

ESQPT in the quantum domain. A main signature of ESQPTs is the divergence of the density of states at an energy denoted by E_{ESQPT} . In the mean-field approximation, it has been shown that this energy coincides with the energy of the classical system at the saddle point [67,68], that is, for the LMG model, $E_{\text{ESQPT}}^{\text{LMG}}/j = h_{\text{LMG}}(\mathbf{x}_1) = e_1 = \sqrt{1 + \Omega_x^2}$. In Fig. 6, we show the density of states for the LMG model taking $j = 256$ and the parameters of Fig. 5(a). These parameters correspond to the unstable region where there is a nonzero Lyapunov exponent (see Fig. 4). The divergence in the density of states associated with the ESQPT is clearly visible at $e_1 = 1.265$, marked with a vertical red dashed line.

IV. GEOMETRY OF THE PARAMETER SPACE OF THE LMG MODEL

In this section, we study the geometry of the ground and the highest-energy states of the LMG model. Although the semiclassical analysis performed above employing $SU(2)$ coherent states provides rich and valuable information about the system, its stationary points, and its quantum phases, it is not well suited to study the geometry of the parameter space of this system. As shown in the Appendix, the metric obtained employing coherent states is ill defined for $\xi_y \leq \frac{\sqrt{1 + \Omega_x^2}}{2}$. In this case, the coherent states that describe the ground state and the highest-energy state are given by \mathbf{x}_1 and \mathbf{x}_2 , shown in Eqs. (13) and (14), respectively. In both cases the states have no dependence in the Hamiltonian parameter ξ_y , having null derivatives respect to this parameter.

To overcome this difficulty, for each of these states, we first compute the QMT and its scalar curvature in the thermodynamic limit via the truncated Holstein-Primakoff transformation [75]. This approximation becomes exact for extremal states in this limit but has spurious divergences close to a phase transition [76]. We also carry out an exact diagonalization and compare the analytic and numeric results. In what follows, we take $x = \{x^i\} = (\Omega_x, \xi_y)$ as the adiabatic parameters.

A. Ground state

We begin our analysis with the ground state, which corresponds via the classical Hamiltonian (11) to the stationary

point $\mathbf{x}_2 = (\theta_2, \phi_2) = (\arccos \frac{1}{\sqrt{1 + \Omega_x^2}}, \pi)$. The first step is to align the classical pseudospin of the ground-state $\vec{J} = (j \sin \theta_2 \cos \phi_2, j \sin \theta_2 \sin \phi_2, j \cos \theta_2)$ with the z axis. To do this, we perform a rotation of the spin operators around the y axis as follows [77]:

$$\begin{pmatrix} \hat{J}_x \\ \hat{J}_y \\ \hat{J}_z \end{pmatrix} = \begin{pmatrix} \cos \theta_2 & 0 & \sin \theta_2 \\ 0 & 1 & 0 \\ -\sin \theta_2 & 0 & \cos \theta_2 \end{pmatrix} \begin{pmatrix} \hat{J}'_x \\ \hat{J}'_y \\ \hat{J}'_z \end{pmatrix}. \quad (20)$$

With this rotation, the Hamiltonian (8) takes the form

$$\hat{H} = \sqrt{1 + \Omega_x^2} \hat{J}'_z + \frac{\xi_y}{j} \hat{J}'_y^2, \quad (21)$$

which is suitable for applying the Holstein-Primakoff transformation that maps angular momentum operators into bosonic operators as

$$\begin{aligned} \hat{J}'_z &= \hat{a}^\dagger \hat{a} - j, & \hat{J}'_+ &= \hat{a}^\dagger (2j - \hat{a}^\dagger \hat{a})^{1/2}, \\ \hat{J}'_- &= (2j - \hat{a}^\dagger \hat{a})^{1/2} \hat{a}. \end{aligned} \quad (22)$$

It is readily verified that this representation satisfies the $SU(2)$ algebra as long as $[\hat{a}, \hat{a}^\dagger] = 1$. Now, we consider the thermodynamic limit $j \rightarrow \infty$ and expand the square roots retaining only the zeroth-order term in $1/j$ [33,77]. The Cartesian components of the angular momentum turn out to be

$$\begin{aligned} \hat{J}'_x &\simeq \sqrt{\frac{j}{2}} (\hat{a}^\dagger + \hat{a}), & \hat{J}'_y &\simeq -i \sqrt{\frac{j}{2}} (\hat{a}^\dagger - \hat{a}), \\ \hat{J}'_z &= \hat{a}^\dagger \hat{a} - j. \end{aligned} \quad (23)$$

In principle, we may substitute these expressions into Eq. (21) and perform a Bogoliubov transformation to creation and annihilation operators (\hat{b}, \hat{b}^\dagger) that diagonalize the Hamiltonian. However, for illustrative purposes, we make first the intermediate transformation $\hat{Q} = \frac{1}{\sqrt{2}} (\hat{a}^\dagger + \hat{a})$, $\hat{P} = \frac{i}{\sqrt{2}} (\hat{a}^\dagger - \hat{a})$ to find that the Hamiltonian takes the form

$$\hat{H} \simeq -j \sqrt{1 + \Omega_x^2} + \left(\frac{\sqrt{1 + \Omega_x^2} + 2\xi_y}{2} \right) \hat{P}^2 + \frac{\sqrt{1 + \Omega_x^2}}{2} \hat{Q}^2. \quad (24)$$

This suggests the use of the following transformation:

$$\begin{aligned} \hat{Q} &= \left(\frac{\sqrt{1 + \Omega_x^2} + 2\xi_y}{4\sqrt{1 + \Omega_x^2}} \right)^{1/4} (\hat{b}^\dagger + \hat{b}), \\ \hat{P} &= i \left(\frac{\sqrt{1 + \Omega_x^2}}{4(\sqrt{1 + \Omega_x^2} + 2\xi_y)} \right)^{1/4} (\hat{b}^\dagger - \hat{b}), \end{aligned} \quad (25)$$

which will cast the Hamiltonian (24) into the harmonic oscillator,

$$\hat{H} \simeq -j \sqrt{1 + \Omega_x^2} + \sqrt{\sqrt{1 + \Omega_x^2} (\sqrt{1 + \Omega_x^2} + 2\xi_y)} \left(\hat{b}^\dagger \hat{b} + \frac{1}{2} \right), \quad (26)$$

where $\omega = \sqrt{\sqrt{1 + \Omega_x^2} (\sqrt{1 + \Omega_x^2} + 2\xi_y)}$ is the frequency and $E = -j \sqrt{1 + \Omega_x^2}$ is the energy. The QMT can now be calculated with the aid of Eq. (2), setting $n = 0$, and employing the

operators,

$$\begin{aligned} \frac{\partial \hat{H}_{\text{LMG}}}{\partial \Omega_x} &= \hat{J}_x = \frac{1}{\sqrt{1 + \Omega_x^2}} \hat{J}'_x + \frac{\Omega_x}{\sqrt{1 + \Omega_x^2}} \hat{J}'_z, \\ \frac{\partial \hat{H}_{\text{LMG}}}{\partial \xi_y} &= \frac{\hat{J}'_y}{j} = \frac{\hat{J}'_y{}^2}{j} \end{aligned} \quad (27)$$

provided that they are expressed in terms of $(\hat{b}, \hat{b}^\dagger)$ to act on the eigenstates of \hat{H} . We find the metric components,

$$\begin{aligned} g_{11} &= \frac{j}{2(\Omega_x^2 + 1)^{7/4} \sqrt{\sqrt{\Omega_x^2 + 1} + 2\xi_y}} \\ &\quad + \frac{\xi_y^2 \Omega_x^2}{8(\Omega_x^2 + 1)^2 (\sqrt{\Omega_x^2 + 1} + 2\xi_y)^2}, \\ g_{12} &= -\frac{\xi_y \Omega_x}{8(\Omega_x^2 + 1) (\sqrt{\Omega_x^2 + 1} + 2\xi_y)^2}, \\ g_{22} &= \frac{1}{8(\sqrt{\Omega_x^2 + 1} + 2\xi_y)^2}, \end{aligned} \quad (28)$$

and the determinant,

$$g = \frac{j}{16(\Omega_x^2 + 1)^{7/4} (\sqrt{\Omega_x^2 + 1} + 2\xi_y)^{5/2}}. \quad (29)$$

Note that a singularity appears in all the components when $\xi_y = -\frac{\sqrt{\Omega_x^2 + 1}}{2}$. Also, we observe that g_{11} consists of two terms, one of them is proportional to j and dominant as $j \rightarrow \infty$. Retaining all the terms and using Eq. (6), we find that the scalar curvature associated with the metric (29) simplifies to

$$R = -4. \quad (30)$$

Remarkably, the scalar curvature is constant despite the nontrivial dependence of the metric components on the parameters. Furthermore, there is no sign of the singularity that appeared in the metric, implying that this singularity is not revealed in the parameter space's intrinsic geometry. We must mention that if we had considered only the dominant term in j in g_{11} for the computation of the scalar curvature, the result would have been different; therefore, we chose to retain all the terms. This constant negative curvature signals that the ground state's parameter space possesses a hyperbolic geometry and is isomorphic to the Lobachevskij space [78].

In Fig. 7 we plot the metric components and the scalar curvature for $\xi_y = 2.3$ and $j = 120$. We see that the numeric results agree well with their analytic counterparts coming from the Holstein-Primakoff approximation. Figure 8 shows a map of the scalar curvature for different values of j where we see a tendency to the analytic result as j increases. Note that the singularity predicted by the metric components (29) is outside the range of the parameters employed in this paper ($\xi_y \geq 0$).

B. Highest-energy state

We now study the highest-energy state for which the QPT occurs. We divide the parameter space into regions above and

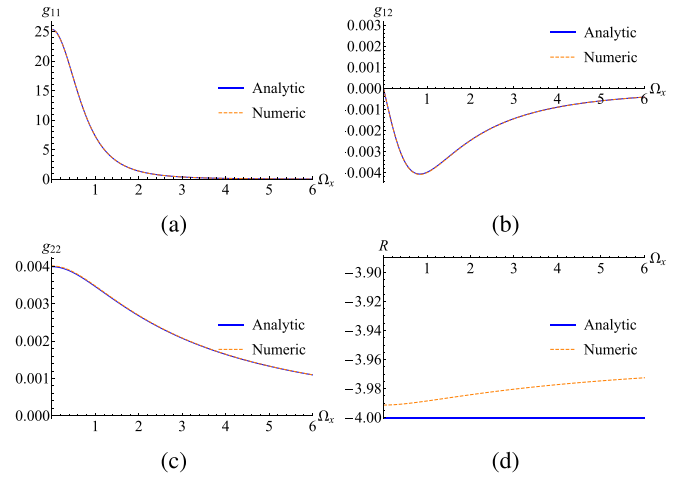


FIG. 7. QMT and its scalar curvature for the ground state when $j = 120$ and $\xi_y = 2.3$.

below the separatrix and, thus, treat each phase separately. The energy of the maximum is

$$\frac{E_{\max}}{j} = \begin{cases} \frac{1 + \Omega_x^2 + 4\xi_y^2}{4\xi_y}, & \Omega_x < \Omega_{xc}, \\ \sqrt{1 + \Omega_x^2}, & \Omega_x \geq \Omega_{xc}, \end{cases} \quad (31)$$

where $\Omega_{xc} = \sqrt{4\xi_y^2 - 1}$ is the critical value of Ω_x (for a fixed ξ_y). The energy E_{\max} and its first derivative are continuous as a function of Ω_x at the stationary point $\Omega_x = \Omega_{xc}$, whereas its second derivative presents a discontinuity. This signals a second-order QPT.

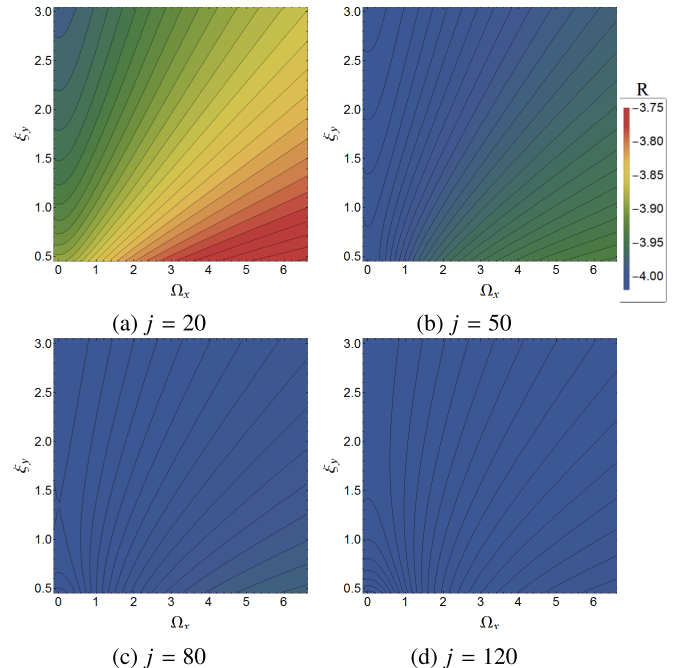


FIG. 8. Scalar curvature map for different values of j , all in the ground state.

1. Symmetric phase

We begin with the parameter space below the separatrix, i.e., when $\xi_y < \frac{\sqrt{1+\Omega_x^2}}{2}$ where the procedure to find the QMT is similar to that of the ground state. The angular coordinates of the corresponding stationary point (the red one in Fig. 5) are $(\theta_1, \phi_1) = [\arccos(\frac{1}{\sqrt{1+\Omega_x^2}}), 0]$, and the rotation that aligns the classical pseudospin with the z axis is

$$\begin{pmatrix} \hat{J}_x \\ \hat{J}_y \\ \hat{J}_z \end{pmatrix} = \begin{pmatrix} \cos \theta_1 & 0 & -\sin \theta_1 \\ 0 & 1 & 0 \\ \sin \theta_1 & 0 & \cos \theta_1 \end{pmatrix} \begin{pmatrix} \hat{J}'_x \\ \hat{J}'_y \\ \hat{J}'_z \end{pmatrix}. \quad (32)$$

Making use of the truncated Holstein-Primakoff transformation, we arrive at the quadratic Hamiltonian,

$$\hat{H} \simeq j\sqrt{1+\Omega_x^2} - \left(\frac{\sqrt{1+\Omega_x^2} - 2\xi_y}{2}\right)\hat{P}^2 - \frac{\sqrt{1+\Omega_x^2}}{2}\hat{Q}^2, \quad (33)$$

which describes a harmonic oscillator with frequency $\omega = \sqrt{\sqrt{1+\Omega_x^2}(\sqrt{1+\Omega_x^2} - 2\xi_y)}$ and zero-point energy $E = j\sqrt{1+\Omega_x^2}$. Note that there is a minus sign in the last two terms of Eq. (33) due to this stationary point being a maximum of energy. The components of the metric are

$$\begin{aligned} g_{11} &= \frac{j}{2(\Omega_x^2 + 1)^{7/4} \sqrt{\sqrt{\Omega_x^2 + 1} - 2\xi_y}} \\ &\quad + \frac{\xi_y^2 \Omega_x^2}{8(\Omega_x^2 + 1)^2 (\sqrt{\Omega_x^2 + 1} - 2\xi_y)^2}, \\ g_{12} &= -\frac{\xi_y \Omega_x}{8(\Omega_x^2 + 1) (\sqrt{\Omega_x^2 + 1} - 2\xi_y)^2}, \\ g_{22} &= \frac{1}{8(\sqrt{\Omega_x^2 + 1} - 2\xi_y)^2}, \end{aligned} \quad (34)$$

and the determinant is

$$g = \frac{j}{16(\Omega_x^2 + 1)^{7/4} (\sqrt{\Omega_x^2 + 1} - 2\xi_y)^{5/2}}. \quad (35)$$

We can easily identify a singularity in all the components of the metric and the determinant which occurs at $\xi_y = \frac{\sqrt{1+\Omega_x^2}}{2}$. This is precisely the stationary point where the QPT takes place and confirms the usefulness of the QMT to detect a quantum phase transition. With the QMT (35) at hand, we compute its scalar curvature and find

$$R = -4, \quad (36)$$

which again means that the underlying geometry is hyperbolic.

2. Broken-symmetry phase

Above the separatrix, i.e., when $\xi_y > \frac{\sqrt{1+\Omega_x^2}}{2}$, the angular coordinates of the stationary points (the blue ones in Fig. 5) are $(\theta_4, \phi_4) = [\arccos(\frac{1}{2\xi_y}), \arccos(\frac{\Omega_x}{\sqrt{4\xi_y^2 - 1}})]$, and the rota-

tion that aligns the classical pseudospin with the z axis is

$$\begin{pmatrix} \hat{J}_x \\ \hat{J}_y \\ \hat{J}_z \end{pmatrix} = \begin{pmatrix} \cos \phi_4 & -\sin \phi_4 & 0 \\ \sin \phi_4 & \cos \phi_4 & 0 \\ 0 & 0 & 1 \end{pmatrix} \times \begin{pmatrix} \cos \theta_4 & 0 & -\sin \theta_4 \\ 0 & 1 & 0 \\ \sin \theta_4 & 0 & \cos \theta_4 \end{pmatrix} \begin{pmatrix} \hat{J}'_x \\ \hat{J}'_y \\ \hat{J}'_z \end{pmatrix}. \quad (37)$$

Following similar steps, we find that the quadratic Hamiltonian now is

$$\begin{aligned} \hat{H} \simeq j \frac{4\xi_y^2 + \Omega_x^2 + 1}{4\xi_y} - \frac{\xi_y(4\xi_y^2 - \Omega_x^2 - 1)}{4\xi_y^2 - 1} \hat{P}^2 \\ + \frac{\Omega_x \sqrt{4\xi_y^2 - \Omega_x^2 - 1}}{2(4\xi_y^2 - 1)} (\hat{Q}\hat{P} + \hat{P}\hat{Q}) \\ - \frac{16\xi_y^4 - 8\xi_y^2 + \Omega_x^2 + 1}{4\xi_y(4\xi_y^2 - 1)} \hat{Q}^2. \end{aligned} \quad (38)$$

This Hamiltonian has the form of a generalized harmonic oscillator. In order to remove the crossed term in \hat{Q} and \hat{P} , we perform the further linear canonical transformation,

$$\begin{aligned} \hat{Q} &= \sqrt{\frac{2\xi_y(4\xi_y^2 - \Omega_x^2 - 1)}{4\xi_y^2 - 1}} \hat{Q}', \\ \hat{P} &= \sqrt{\frac{4\xi_y^2 - 1}{2\xi_y(4\xi_y^2 - \Omega_x^2 - 1)}} \hat{P}' + \frac{\Omega_x}{\sqrt{2\xi_y(4\xi_y^2 - 1)}} \hat{Q}'. \end{aligned} \quad (39)$$

The Hamiltonian then also turns into a harmonic oscillator except for a sign,

$$\hat{H} = j \frac{4\xi_y^2 + \Omega_x^2 + 1}{4\xi_y} - \frac{\hat{P}'^2}{2} - \frac{\omega^2}{2} \hat{Q}'^2, \quad (40)$$

with frequency $\omega = \sqrt{4\xi_y^2 - \Omega_x^2 - 1}$ and zero-point energy $E = j \frac{4\xi_y^2 + \Omega_x^2 + 1}{4\xi_y}$. The expressions for the metric components are cumbersome; however, it can be seen that all of them are singular at points on the separatrix. Finally, the computation of the scalar curvature via Eq. (6) also yields a complicated and not illuminating expression.

In Fig. 9, we show the QMT and its scalar curvature and compare them with their numeric counterparts. Good agreement is observed between the analytic and the numeric results. The exception is the g_{11} component, which exhibits a maximum in the numerical calculations at $\Omega_x = 0$ which is not predicted by the Holstein-Primakoff approximation. It seems to be related with the crossover in the projection of \hat{J}_x when Ω_x changes sign as can be seen in Fig. 3, which is clearly detected by g_{11} but does not affect the scalar curvature, which approaches zero in the broken phase both in the analytic and in the numerical analyses. The numerical evaluation of the metric demands high precision due to the near degeneracy of the eigenvalues. To handle this issue specially designed computational techniques are required [79].

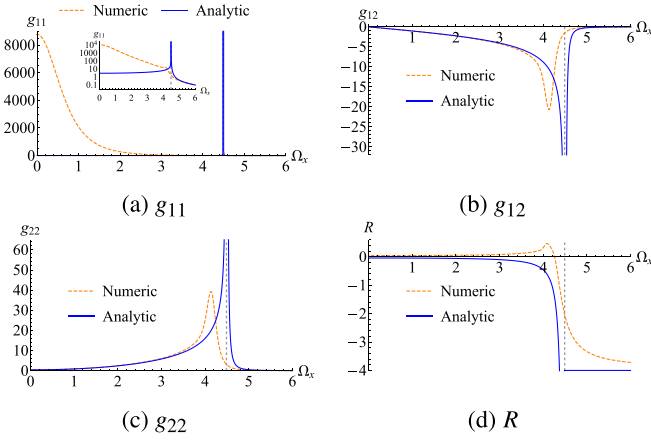


FIG. 9. Comparison of the numeric QMT components and the scalar curvature with the analytic results for $\xi_y = 2.3$ and $j = 96$ for the highest-energy state. The inset shows the g_{11} component on the logarithmic scale. The agreement is excellent except near the QPT (dashed gray). Note in the plots of g_{11} the difference between the analytical and the numerical curves as $\Omega_x \rightarrow 0$.

The broken phase exhibits a Berry curvature, whose only component is given by

$$F_{12} = -\frac{2j + 1}{4\xi_y^2 \sqrt{4\xi_y^2 - \Omega_x^2 - 1}} + \frac{16\xi_y^2 - \Omega_x^2 + 1}{16\xi_y^3 (4\xi_y^2 - \Omega_x^2 - 1)}. \quad (41)$$

We observe as expected that the Berry curvature is also singular at the separatrix. On the other hand, the numeric analysis yields a zero Berry curvature. This discrepancy is a consequence of the rotation performed to align the highest-energy state with the classical pseudospin, which introduced the crossed term in \hat{Q} and \hat{P} in Eq. (38). In the numerical calculations we would obtain a no vanishing Berry curvature rotating the collective pseudospin operators in Hamiltonian (8) to have a linear term in J_y as has been performed in Refs. [80,81].

In Fig. 10, the plots of the numeric QMT components and the scalar curvature for the highest-energy state are shown in three dimensions, whereas Fig. 11 contains their maps. We see that in the regular region where the Lyapunov exponent vanishes, the scalar curvature has a value around -4 , just as the Holstein-Primakoff calculation predicts. However, near the region with a positive Lyapunov exponent, the scalar curvature begins to grow, passes the separatrix, takes small positive values, and reaches a maximum until it descends to near-zero values. Moreover, as the size of the system increases, the peak gets closer to the separatrix, and the transition region between the asymptotic values -4 on one side and 0 on the other side becomes thinner.

How can we interpret the change in sign near the separatrix? Does it mean that there is a change in the topology of the parameter space and that it switches between a closed and an open shape? In order to answer this, we must recall that a fundamental quantity in the study of two-dimensional surfaces is the Gaussian curvature K , which is related to the scalar curvature as $K = R/2$. It is defined as the product of the two principal curvatures κ_1 and κ_2 , which quantify the bending of the surface along each direction [82]. If both principal

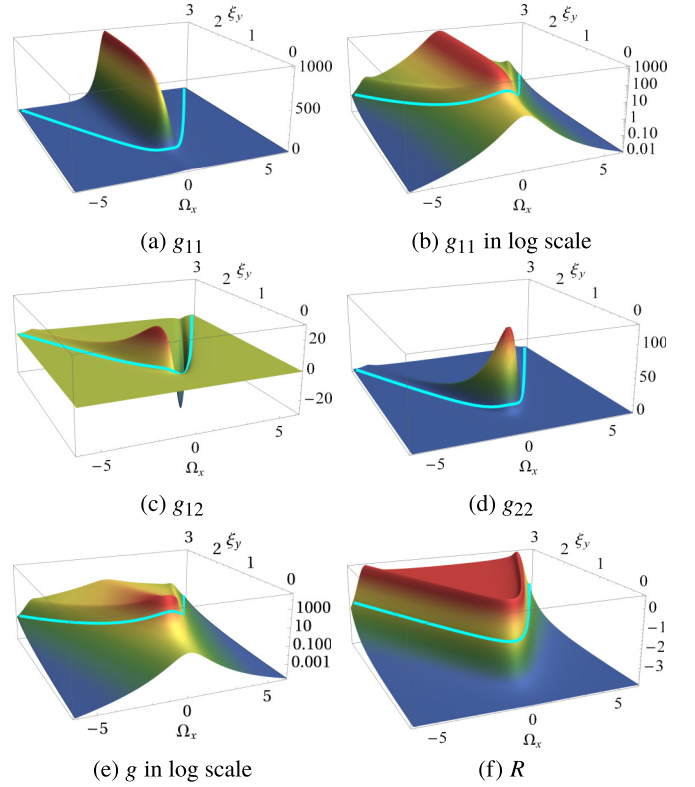


FIG. 10. QMT components and scalar curvature for the highest-energy state with $j = 32$. The cyan line is the separatrix given in Fig. 5(a) when $\xi_y = \frac{\sqrt{1+\Omega_x^2}}{2}$.

curvatures κ_1 and κ_2 have the same sign, then the Gaussian curvature is positive, and the local geometry is spherical. On the contrary, when both principal curvatures have opposite signs, the Gaussian curvature is negative, and the surface is

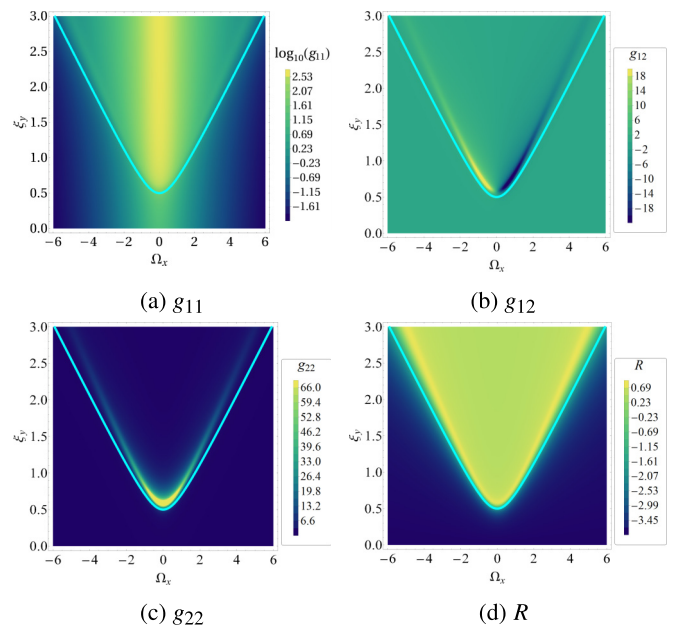


FIG. 11. Maps of the QMT components and the scalar curvature for the highest-energy state with $j = 32$.

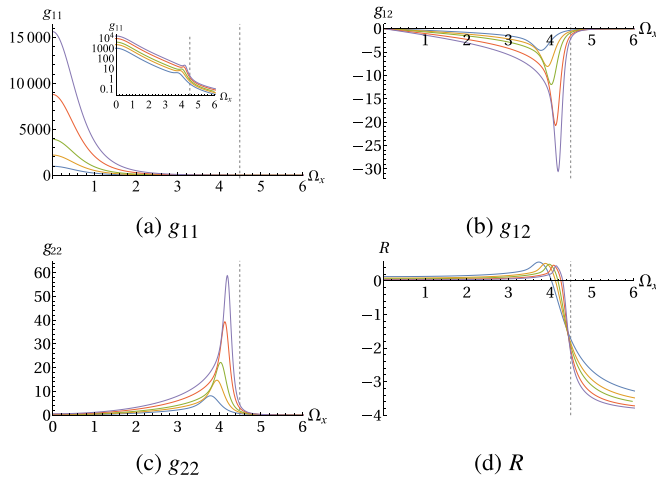


FIG. 12. QMT components and scalar curvature for $\xi_y = 2.3$ and $j = 32, 48, 64, 96, 128$. The inset shows the g_{11} component on the logarithmic scale.

locally hyperbolic. A change in topology would imply that the metric becomes singular at some point, which means that its determinant should vanish there [83]. Since we do not observe that the metric determinant is equal to zero (see Fig. 10), we conclude that a change in topology does not take place. Instead, there is only a change in sign in one of the two principal curvatures κ_1 or κ_2 , producing a local change between domelike and saddlelike shapes.

In Fig 12, the plots of the numeric QMT and its scalar curvature are shown for various j 's when $\xi_y = 2.3$. We can see how the peaks in the metric components and the curvature get closer to the critical value $\Omega_{xc} = 4.490$ as j increases. Also, the peaks become sharper, indicating that, in the thermodynamic limit $j \rightarrow \infty$, the curvature's maximum will be identified with the change in sign of the curvature, indicating these two features as distinctive of the phase transition. In the next section, we carry out an analysis to extract more relevant information about this behavior.

C. Analysis of the peaks

In this section, we analyze the (positive or negative) peaks that are present in the numeric QMT components and the scalar curvature.

1. $\xi_y = 2.3$

In Fig. 13, we plot the extrema (maximum or minimum) of every metric component and of the scalar curvature as a function of Ω_x for $\xi_y = 2.3$ and increasing values of j . The functions used to fit the data are as follows:

$$\begin{aligned} g_{11}^{\max} &= 0.582 + \frac{2.051}{(\Omega_x - 4.490)^2}, \\ g_{12}^{\min} &= 2.249 - \frac{2.966}{(\Omega_x - 4.490)^2}, \\ g_{22}^{\max} &= -7.170 + \frac{5.931}{(\Omega_x - 4.490)^2}, \\ R^{\max} &= -0.083 + 2.470e^{-0.356\Omega_x}. \end{aligned} \quad (42)$$

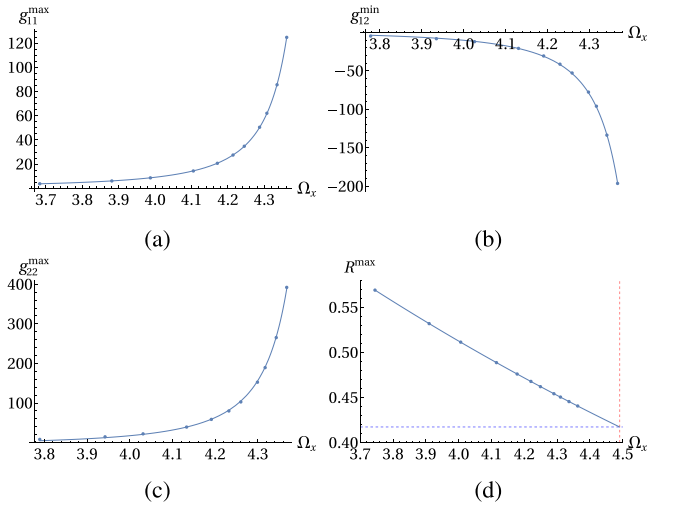


FIG. 13. Behavior of the maximum of each metric component and scalar curvature with respect to Ω_x for $\xi_y = 2.3$. The points correspond to $j = 32, 48, 64, 96, 128, 160, 192, 256, 300, 384, 512$.

We see that at the stationary point $\Omega_{xc} = 4.490$, the metric components are singular, just as the analytic formulas (35) predict. On the other hand, the maximum of the scalar curvature at the stationary point takes the value of 0.416. This is an indication that the maximum of the scalar curvature persists in the thermodynamic limit.

Next, in Fig. 14, we show the peaks of QMT components and the scalar curvature as functions of j . In this case, the functions used to fit the data are as follows:

$$\begin{aligned} \ln(g_{11}^{\max}) &= -3.102 + 1.267 \ln(j), \\ \ln(g_{12}^{\min}) &= -3.134 + 1.349 \ln(j), \\ \ln(g_{22}^{\max}) &= -2.702 + 1.394 \ln(j), \\ R^{\max} &= 0.418 + \frac{1.563}{(j - 0.913)^{0.680}}. \end{aligned} \quad (43)$$

In the thermodynamic limit, $j \rightarrow \infty$, the metric components diverge, whereas the scalar curvature approaches 0.418. This confirms that R is not singular across the QPT, although it has a discontinuity as the tendency in Fig. 12 shows. As a consequence, it can be said that the singularity that appears in

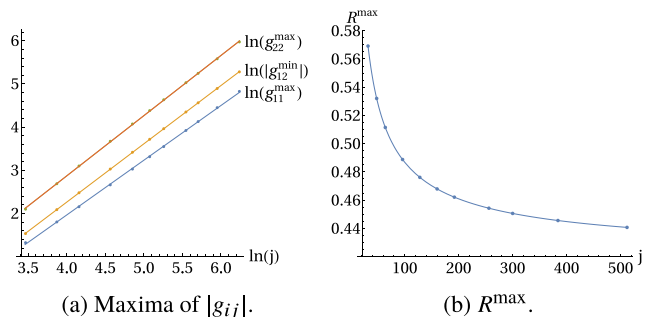


FIG. 14. Maximum of each metric component and the scalar curvature with respect to j for $\xi_y = 2.3$.

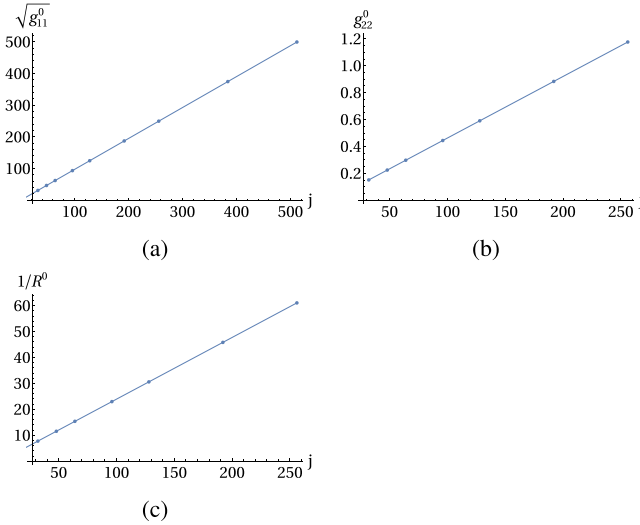


FIG. 15. Plots of g_{11} , g_{22} , and R as functions of j for $\Omega_x = 0$ and $\xi_y = 2.3$.

the metric is removable and it is not a true singularity of the parameter space.

2. $\Omega_x = 0$

Now, we analyze the value of the metric components g_{11} and g_{22} , as well as the scalar curvature when $\Omega_x = 0$. The plots are shown in Fig. 15 and the functions that fit the data are as follows:

$$\begin{aligned} g_{11}^0 &= (-0.013 + 0.976j)^2, \\ g_{22}^0 &= 0.005 + 0.005j, \\ R^0 &= \frac{1}{0.131 + 0.238j}. \end{aligned} \quad (44)$$

Note that g_{12} does not appear because its value at $\Omega_x = 0$ is zero. Remarkably, the scalar curvature goes to 0 as $j \rightarrow \infty$, which is precisely the prediction of the coherent-state approach of the Appendix [see Eq. (A6)].

3. $\xi_y = 0.5$

Finally, in Fig. 16, we show the peaks of the metric components g_{11} and g_{22} as well as the scalar curvature for $\xi_y = 0.5$ as functions of j . This case is particularly interesting since at

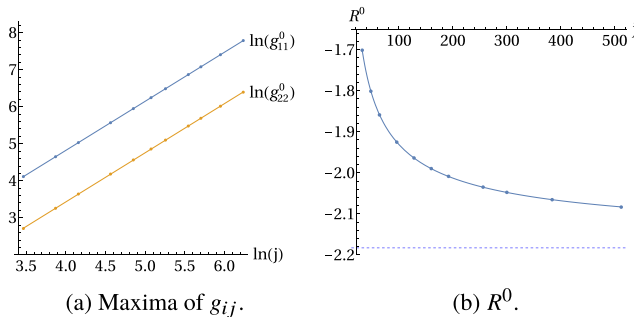


FIG. 16. Maximum of each metric component and the scalar curvature with respect to j for $\xi_y = 0.5$.

$\xi_y = 0.5$ the peaks of the QMT and the scalar curvature occur at $\Omega_x = 0$, regardless of the value of j . The functions used to fit the data in Fig. 16 are as follows:

$$\begin{aligned} \ln(g_{11}^0) &= -0.480 + 1.325 \ln(j), \\ \ln(g_{22}^0) &= -1.881 + 1.327 \ln(j), \\ R^0 &= -2.183 + \frac{3.430}{(j^2 - 6.206)^{0.284}}. \end{aligned} \quad (45)$$

In this case, in the thermodynamic limit $j \rightarrow \infty$, the metric components also diverge, whereas the scalar curvature approaches -2.183 . This is a limiting point over the separatrix where the scalar curvature takes an intermediate value between the asymptotic ones in the two phases (0 and -4). Once again, this confirms that R is not singular across the QPT, and there is not a true singularity at this point in the parameter space.

V. CONCLUSIONS

In this paper, we have studied the geometry of the parameter space of a LMG model. The LMG model that we chose has a nondegenerate metric across the parameter space as opposed to that considered in Ref. [20] where the quantum metric was obtained only for the symmetric phase of the model and the other phase was not studied due to the vanishing metric determinant. This model allowed us to compute the scalar curvature in both phases.

After introducing the QMT and the scalar curvature, which contain the relevant geometric information, we carried out a classical mean-field analysis employing Bloch coherent states. This analysis allowed the determination of the Hamiltonian stationary points and their classification according to their stability properties. Two points were of relevance in our paper: the ground state and the highest-energy state. The first state did not show any singular behavior in the parameter space under consideration ($\xi_y > 0$). On the other hand, the second state exhibited a QPT, and as a result, the QMT components turned out singular. Both states were studied from an analytic and a numeric perspective. The analytic treatment was performed under the truncated Holstein-Primakoff transformation, which yields a quadratic approximation to the system near the chosen state. The numeric computation used the original Hamiltonian and employed exact diagonalization to extract the QMT and then numerical differentiation over a mesh to find the scalar curvature.

The analytic and numeric results match for the ground state. On the other hand, the g_{11} component of the numeric QMT for the highest-energy state shows a peak for small values of Ω_x , which the analytic counterpart does not possess. The reason for this behavior may be related to the fact that the classical system is not invariant under $Q \rightarrow -Q$, i.e., it has a broken symmetry as can be seen in Eq. (11) and is related to the crossover in the projection of \hat{J}_x for the change in sign of Ω_x , indicated in Fig. 3. In contrast to this, the analytic computation is carried out under the truncated Holstein-Primakoff approximation, which yields a quadratic Hamiltonian possessing the $Q \rightarrow -Q$ symmetry. Another difference between the analytic and the numeric results is the appearance of a Berry

curvature in the analytic case, which also detects the QPT but is not present in the numeric case. The same Berry curvature could be obtained in the numerical calculations rotating the collective pseudospin operators in the Hamiltonian (8).

For the highest-energy state, we find that far from the separatrix, both the analytic and the numeric results show that the scalar curvature takes the value of -4 in the symmetric phase. In the broken-symmetry phase, the scalar curvature tends to zero in the thermodynamic limit $j \rightarrow \infty$. In this limit, the metric components diverge over the separatrix, whereas the scalar curvature R always takes finite values across the QPT in the numerical calculations. This contrasts with its singular behavior predicted employing the truncated Holstein-Primakoff, which becomes unreliable in close vicinity of the phase transition. We conclude that the singularity appearing in the metric is removable and is not a true singularity of the parameter space. However, in terms of the scalar curvature, the second-order QPT is indicated as a sudden change in sign.

ACKNOWLEDGMENTS

We acknowledge support of the Computation Center-ICN, in particular, of E. Palacios, L. Díaz, and E. Murrieta. D.G.-R. was supported by CONACyT Ph.D. Scholarship No. 332577. D.G. was partially supported by a DGAPA-UNAM postdoctoral fellowship and by Consejo Nacional de Ciencia y Tecnología (CONACyT), México, Grant No. A1-S-7701. J.C.-C. was supported by a DGAPA-UNAM postdoctoral fellowship. This work was partially supported by DGAPA-PAPIIT Grants No. IN103919 and IN104020.

APPENDIX: BLOCH COHERENT STATES

The $SU(2)$ coherent states are parametrized by the complex number $z = \tan \frac{\theta}{2} e^{-i\phi}$ and are given by

$$|z\rangle = \frac{e^{z\hat{J}_+} |j, -j\rangle}{(1 + |z|^2)^j} = \sum_{m=-j}^j c_m^{(j)} |j, m\rangle, \quad (\text{A1})$$

where

$$c_m^{(j)} := \binom{2j}{j+m}^{1/2} \sin^{j+m} \frac{\theta}{2} \cos^{j-m} \frac{\theta}{2} e^{-i(j+m)\phi}. \quad (\text{A2})$$

The angles on the Bloch sphere are functions of the parameters, i.e., $\theta = \theta(x)$ and $\phi = \phi(x)$ with $x = (\Omega_x, \xi_y)$. The coherent state of the maximum has the coordinates:

$$(1) \quad (\theta_4, \phi_4) = \left[\arccos\left(-\frac{1}{2\xi_y}\right), \arccos\left(-\frac{\Omega_x}{\sqrt{4\xi_y^2 - 1}}\right) \right]$$

$$\text{for } \xi_y > \frac{\sqrt{1 + \Omega_x^2}}{2}.$$

$$(2) \quad (\theta_1, \phi_1) = \left[\arccos\left(-\frac{1}{\sqrt{1 + \Omega_x^2}}\right), 0 \right]$$

$$\text{for } \xi_y \leq \frac{\sqrt{1 + \Omega_x^2}}{2}.$$

Therefore, the classical angular momentum vector is given by $\vec{J} = j(\sin \theta \cos \phi, \sin \theta \sin \phi, \cos \theta)$.

The quantum geometric tensor for the coherent state $|z\rangle$ is given by

$$\begin{aligned} Q_{ij}^{(z)} &= \langle \partial_i z | \partial_j z \rangle - \langle \partial_i z | z \rangle \langle z | \partial_j z \rangle \\ &= \sum_{m=-j}^j \partial_i c_m^{*(j)} \partial_j c_m^{(j)} - \sum_{m=-j}^j \partial_i c_m^{*(j)} c_m^{(j)} \sum_{n=-j}^j c_n^{*(j)} \partial_j c_n^{(j)}. \end{aligned} \quad (\text{A3})$$

With this at hand, we find the metric tensor, its determinant, and the Berry curvature for both phases.

(1) For $\xi_y > \frac{\sqrt{1 + \Omega_x^2}}{2}$,

$$\begin{aligned} F_{12}^{(z)} &= -\frac{j}{2} \frac{1}{\xi_y^2 \sqrt{4\xi_y^2 - \Omega_x^2 - 1}}, \\ g_{11}^{(z)} &= \frac{j}{2} \frac{4\xi_y^2 - 1}{4\xi_y^2 (4\xi_y^2 - \Omega_x^2 - 1)}, \\ g_{12}^{(z)} &= -\frac{j}{2} \frac{\Omega_x}{\xi_y (4\xi_y^2 - \Omega_x^2 - 1)}, \\ g_{22}^{(z)} &= \frac{j}{2} \frac{\Omega_x^2 + 1}{\xi_y^2 (4\xi_y^2 - \Omega_x^2 - 1)}, \\ g^{(z)} &= \frac{j^2}{16\xi_y^4 (4\xi_y^2 - \Omega_x^2 - 1)}. \end{aligned} \quad (\text{A4})$$

(2) For $\xi_y \leq \frac{\sqrt{1 + \Omega_x^2}}{2}$,

$$\begin{aligned} F_{12}^{(z)} &= 0, \quad g_{11}^{(z)} = \frac{j}{2} \frac{1}{(\Omega_x^2 + 1)^2}, \\ g_{12}^{(z)} &= 0, \quad g_{22}^{(z)} = 0, \quad g^{(z)} = 0. \end{aligned} \quad (\text{A5})$$

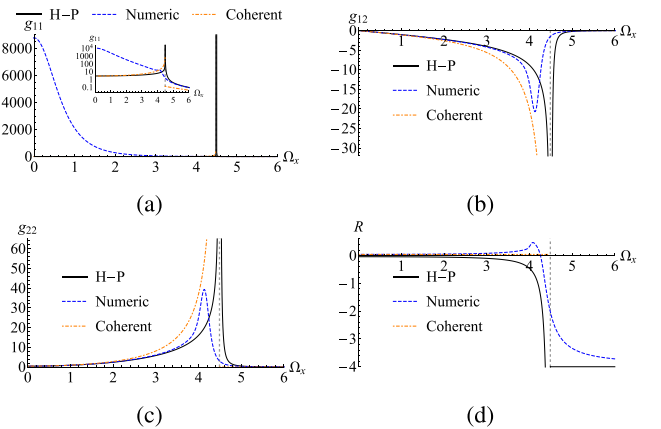


FIG. 17. Comparison of the QGT and R obtained with the truncated Holstein-Primakoff approximation (solid black), coherent states (dot-dashed orange), and exact diagonalization (dashed blue). We fixed $j = 96$ and $\xi_y = 2.3$.

The scalar curvature is only defined above the separatrix (since the metric is invertible in that region) and is given by

$$R = 4/j. \tag{A6}$$

In Fig. 17, we plot the QMT and its scalar curvature obtained through the Bloch coherent states and compare the results with those coming from the truncated Holstein-Primakoff transformation as well as those coming from the exact diagonalization of the Hamiltonian.

[1] A. Carollo, D. Valenti, and B. Spagnolo, *Phys. Rep.* **838**, 1 (2020).

[2] J. P. Provost and G. Vallee, *Commun. Math. Phys.* **76**, 289 (1980).

[3] T. Ozawa and N. Goldman, *Phys. Rev. B* **97**, 201117(R) (2018).

[4] O. Bleu, D. D. Solnyshkov, and G. Malpuech, *Phys. Rev. B* **97**, 195422 (2018).

[5] M. Yu, P. Yang, M. Gong, Q. Cao, Q. Lu, H. Liu, S. Zhang, M. B. Plenio, F. Jelezko, T. Ozawa, N. Goldman, and J. Cai, *Natl. Sci. Rev.* **7**, 254 (2019).

[6] X. Tan, D.-W. Zhang, Z. Yang, J. Chu, Y.-Q. Zhu, D. Li, X. Yang, S. Song, Z. Han, Z. Li, Y. Dong, H.-F. Yu, H. Yan, S.-L. Zhu, and Y. Yu, *Phys. Rev. Lett.* **122**, 210401 (2019).

[7] X. Tan, D.-W. Zhang, Z. Yang, J. Chu, Y.-Q. Zhu, D. Li, X. Yang, S. Song, Z. Han, Z. Li, Y. Dong, H.-F. Yu, H. Yan, S.-L. Zhu, and Y. Yu, *Phys. Rev. Lett.* **123**, 159902(E) (2019).

[8] L. Campos Venuti and P. Zanardi, *Phys. Rev. Lett.* **99**, 095701 (2007).

[9] P. Kumar and T. Sarkar, *Phys. Rev. E* **90**, 042145 (2014).

[10] P. Zanardi, P. Giorda, and M. Cozzini, *Phys. Rev. Lett.* **99**, 100603 (2007).

[11] P. Zanardi and N. Paunković, *Phys. Rev. E* **74**, 031123 (2006).

[12] D. Gonzalez, D. Gutiérrez-Ruiz, and J. D. Vergara, *J. Phys. A: Math. Theor.* **53**, 505305 (2020).

[13] S.-J. Gu, *Int. J. Mod. Phys. B* **24**, 4371 (2010).

[14] W. Rządkowski, N. Defenu, S. Chiacchiera, A. Trombettoni, and G. Bighin, *New J. Phys.* **22**, 093026 (2020).

[15] W. K. Wootters, *Phys. Rev. D* **23**, 357 (1981).

[16] P. Kumar, S. Mahapatra, P. Phukon, and T. Sarkar, *Phys. Rev. E* **86**, 051117 (2012).

[17] M. Tomka, T. Souza, S. Rosenberg, and A. Polkovnikov, *arXiv:1606.05890*.

[18] M. Kolodrubetz, V. Gritsev, and A. Polkovnikov, *Phys. Rev. B* **88**, 064304 (2013).

[19] M. Kolodrubetz, D. Sels, P. Mehta, and A. Polkovnikov, *Phys. Rep.* **697**, 1 (2017).

[20] A. Dey, S. Mahapatra, P. Roy, and T. Sarkar, *Phys. Rev. E* **86**, 031137 (2012).

[21] F. Weinhold, *J. Chem. Phys.* **63**, 2479 (1975).

[22] G. Ruppeiner, *Phys. Rev. A* **20**, 1608 (1979).

[23] G. Ruppeiner, *Rev. Mod. Phys.* **67**, 605 (1995).

[24] G. Ruppeiner, *Rev. Mod. Phys.* **68**, 313 (1996).

[25] O. Castañós, R. López-Peña, E. Nahmad-Achar, and J. G. Hirsch, *J. Phys.: Conf. Ser.* **403**, 012003 (2012).

[26] M. A. Bastarrachea-Magnani, O. Castañós, E. Nahmad-Achar, R. López-Peña, and J. G. Hirsch, *J. Phys.: Conf. Ser.* **492**, 012012 (2014).

[27] G. Sun, A. K. Kolezhuk, and T. Vekua, *Phys. Rev. B* **91**, 014418 (2015).

[28] P. Tomczak, Topological charge scaling at a quantum phase transition, *arXiv:2103.16203*.

[29] L. Cincio, M. M. Rams, J. Dziarmaga, and W. H. Zurek, *Phys. Rev. B* **100**, 081108(R) (2019).

[30] H. Lipkin, N. Meshkov, and A. Glick, *Nucl. Phys.* **62**, 188 (1965).

[31] N. Meshkov, A. Glick, and H. Lipkin, *Nucl. Phys.* **62**, 199 (1965).

[32] A. Glick, H. Lipkin, and N. Meshkov, *Nucl. Phys.* **62**, 211 (1965).

[33] H.-M. Kwok, W.-Q. Ning, S.-J. Gu, and H.-Q. Lin, *Phys. Rev. E* **78**, 032103 (2008).

[34] H. T. Quan and F. M. Cucchietti, *Phys. Rev. E* **79**, 031101 (2009).

[35] O. Castañós, R. López-Peña, E. Nahmad-Achar, and J. G. Hirsch, *J. Phys.: Conf. Ser.* **387**, 012021 (2012).

[36] D. D. Scherer, C. A. Müller, and M. Kastner, *J. Phys. A: Math. Theor.* **42**, 465304 (2009).

[37] M. V. Berry, *J. Phys. A* **18**, 15 (1985).

[38] G. J. Dreiss and A. Klein, *Nucl. Phys. A* **139**, 81 (1969).

[39] P. Schuck and S. Ethofer, *Nucl. Phys. A* **212**, 269 (1973).

[40] F. Catara, N. Dinh Dang, and M. Sambataro, *Nucl. Phys. A* **579**, 1 (1994).

[41] J. M. Wahlen-Strothman, T. M. Henderson, M. R. Hermes, M. Degroote, Y. Qiu, J. Zhao, J. Dukelsky, and G. E. Scuseria, *J. Chem. Phys.* **146**, 054110 (2017).

[42] A. V. Turbiner, *Commun. Math. Phys.* **118**, 467 (1988).

[43] V. Ulyanov and O. Zaslavskii, *Phys. Rep.* **216**, 179 (1992).

[44] R. Botet and R. Jullien, *Phys. Rev. B* **28**, 3955 (1983).

[45] J. I. Cirac, M. Lewenstein, K. Mølmer, and P. Zoller, *Phys. Rev. A* **57**, 1208 (1998).

[46] D. Gatteschi, R. Sessoli, and J. Villain, *Molecular Nanomagnets*, Mesoscopic Physics and Nanotechnology (Oxford University Press, Oxford, 2006).

[47] L. Bogani and W. Wernsdorfer, *Nature Mater.* **7**, 179 (2008).

[48] A. Russomanno, F. Iemini, M. Dalmonte, and R. Fazio, *Phys. Rev. B* **95**, 214307 (2017).

[49] S. Campbell, G. De Chiara, M. Paternostro, G. M. Palma, and R. Fazio, *Phys. Rev. Lett.* **114**, 177206 (2015).

[50] O. L. Acevedo, L. Quiroga, F. J. Rodríguez, and N. F. Johnson, *Phys. Rev. Lett.* **112**, 030403 (2014).

[51] N. Defenu, T. Enss, M. Kastner, and G. Morigi, *Phys. Rev. Lett.* **121**, 240403 (2018).

[52] R. Puebla, A. Smirne, S. F. Huelga, and M. B. Plenio, *Phys. Rev. Lett.* **124**, 230602 (2020).

[53] W. Kopylov, G. Schaller, and T. Brandes, *Phys. Rev. E* **96**, 012153 (2017).

[54] V. Makhalov, T. Satoor, A. Evrard, T. Chalopin, R. Lopes, and S. Nascimbene, *Phys. Rev. Lett.* **123**, 120601 (2019).

[55] S. Dusuel and J. Vidal, *Phys. Rev. Lett.* **93**, 237204 (2004).

- [56] J. Vidal, G. Palacios, and R. Mosseri, *Phys. Rev. A* **69**, 022107 (2004).
- [57] J. I. Latorre, R. Orús, E. Rico, and J. Vidal, *Phys. Rev. A* **71**, 064101 (2005).
- [58] T. Barthel, S. Dusuel, and J. Vidal, *Phys. Rev. Lett.* **97**, 220402 (2006).
- [59] G. Ortiz, R. Somma, J. Dukelsky, and S. Rombouts, *Nucl. Phys. B* **707**, 421 (2005).
- [60] R. Gilmore and D. H. Feng, *Phys. Lett. B* **76**, 26 (1978).
- [61] A. Kuriyama, M. Yamamura, C. Providência, J. da Providência, and Y. Tsue, *J. Phys. A* **36**, 10361 (2003).
- [62] O. Castaños, R. López-Peña, J. G. Hirsch, and E. López-Moreno, *Phys. Rev. B* **72**, 012406 (2005).
- [63] O. Castaños, R. López-Peña, J. G. Hirsch, and E. López-Moreno, *Phys. Rev. B* **74**, 104118 (2006).
- [64] F. Leyvraz and W. D. Heiss, *Phys. Rev. Lett.* **95**, 050402 (2005).
- [65] W. D. Heiss, F. G. Scholtz, and H. B. Geyer, *J. Phys. A* **38**, 1843 (2005).
- [66] P. Ribeiro, J. Vidal, and R. Mosseri, *Phys. Rev. Lett.* **99**, 050402 (2007).
- [67] P. Cejnar, M. Macek, S. Heinze, J. Jolie, and J. Dobeš, *J. Phys. A* **39**, L515 (2006).
- [68] M. Caprio, P. Cejnar, and F. Iachello, *Ann. Phys. (NY)* **323**, 1106 (2008).
- [69] P. Cejnar, J. Jolie, and R. F. Casten, *Rev. Mod. Phys.* **82**, 2155 (2010).
- [70] P. Pérez-Fernández, P. Cejnar, J. M. Arias, J. Dukelsky, J. E. García-Ramos, and A. Relaño, *Phys. Rev. A* **83**, 033802 (2011).
- [71] T. Brandes, *Phys. Rev. E* **88**, 032133 (2013).
- [72] L. F. Santos and F. Pérez-Bernal, *Phys. Rev. A* **92**, 050101(R) (2015).
- [73] L. F. Santos, M. Távora, and F. Pérez-Bernal, *Phys. Rev. A* **94**, 012113 (2016).
- [74] S. Pilatowsky-Cameo, J. Chávez-Carlos, M. A. Bastarrachea-Magnani, P. Stránský, S. Lerma-Hernández, L. F. Santos, and J. G. Hirsch, *Phys. Rev. E* **101**, 010202(R) (2020).
- [75] T. Holstein and H. Primakoff, *Phys. Rev.* **58**, 1098 (1940).
- [76] J. G. Hirsch, O. Castaños, R. López-Peña, and E. Nahmad-Achar, *Phys. Scr.* **87**, 038106 (2013).
- [77] S. Dusuel and J. Vidal, *Phys. Rev. B* **71**, 224420 (2005).
- [78] D. V. Alekseevskij, E. B. Vinberg, and A. S. Solodovnikov, in *Geometry of Spaces of Constant Curvature, Geometry II.*, edited by E. B. Vinberg, Encyclopaedia of Mathematical Sciences, Vol. 29 (Springer, Berlin, 1993).
- [79] 27. Software issues in floating point arithmetic, in *Accuracy and Stability of Numerical Algorithms*, pp. 489–509, <https://epubs.siam.org/doi/pdf/10.1137/1.9780898718027.ch27>.
- [80] H. Cui, K. Li, and X. Yi, *Phys. Lett. A* **360**, 243 (2006).
- [81] Z.-G. Yuan, P. Zhang, S.-S. Li, J. Jing, and L.-B. Kong, *Phys. Rev. A* **85**, 044102 (2012).
- [82] M. Spivak, *A Comprehensive Introduction to Differential Geometry*, Vol. 3 (Publish or Perish, Houston, Texas, 1999).
- [83] S. Hawking, *Nucl. Phys. B* **144**, 349 (1978).